

Observation of quantum phase synchronization in spin-1 atoms

Arif Warsi Laskar,¹ Pratik Adhikary,¹ Suprodip Mondal,¹
Parag Katiyar,¹ Sai Vinjanampathy,^{2,3} and Saikat Ghosh^{1,*}

¹*Department of Physics, Indian Institute of Technology - Kanpur, UP-208016, India*

²*Department of Physics, Indian Institute of Technology-Bombay, Powai, Mumbai 400076, India*

³*Centre for Quantum Technologies, National University of Singapore, 3 Science Drive 2, 117543 Singapore, Singapore*

(Dated: September 3, 2022)

With growing interest in quantum technologies, possibilities of synchronizing quantum systems has garnered significant recent attention. In experiments with dilute ensemble of laser cooled, spin-1 ⁸⁷Rb atoms, we observe quantum phase of atomic coherent state to synchronize with external phases of classical fields. In particular, when we destructively interfere two dark state polaritons in a spin-1 manifold the resulting spin-1 state in phase space gets localized, only in presence of anisotropic decay channels. Furthermore, we observe a blockade of synchronization due to quantum interference and emergence of Arnold tongue-like features, as has been predicted recently. Such decay induced synchronization of spin systems with no classical analogue can provide insights in open quantum systems and find key applications in synchronizing quantum networks.

Examples of spontaneous synchronization, ranging from synchronized light patterns of fire-flies to neuronal activities, are abundant in nature [1]. Such synchronous dynamics, being stable to external perturbations, have also found a wide range of applications in disparate areas of science and engineering, including synchronized satellites [2], high power electrical grid lines [3], clocks [4] and wind turbines [5]. In recent decades, synchronization of quantum systems has emerged as a critical field for understanding interplay between classical dynamics and quantum correlations [6–18] and for applications in quantum networks [6, 19, 20]. Early theoretical proposals focused on open quantum systems whose mean-field theories exhibited synchronization [9, 20–22], when interpolated from classical to quantum regimes. Such nonlinear oscillator models were extended deep in the quantum regime and were compared to inherently quantum, finite dimensional systems that have no classical analogue [11, 15, 23]. In both these systems, suitably chosen angles in phase space of the steady state density matrix were shown to be entrained to the phase of an external signal with quantum interference effects like blockade of synchronization. Despite such proposals, observation of synchronization deep in the quantum regime has remained elusive.

Recently, it was predicted [15, 17] that a spin-1 system with internal decay rates γ_g and γ_d , exhibit synchronization of stable limit-cycle oscillations in phase space (Fig. 1a). The limit-cycle is characterized by a free phase ϕ in the corresponding Husimi-Q representation function [24]. For asymmetric decay rates, this phase is predicted to synchronize to the difference phase of weak classical drives (represented with two coherent couplings $\eta_{-1,0}$, $\eta_{0,1}$, Fig. 1a).

Here we report first observation of quantum synchronization in such spin-1 atoms. The experiment involves a dilute ensemble of approximately a million ⁸⁷Rb atoms, laser cooled and initialized to a ground state

$|F=1, m_F=0\rangle$ (at time instance t_I , Fig. 1c, d and e). This state corresponds to an equatorial limit cycle in Husimi-Q phase space representation. Two circularly polarized *control* fields ($\Omega_{c(S)}^\pm$) along with a π -polarized *probe* field Ω_p^π , induce coherent two-photon couplings between the spin states $|F=1, m_F=\pm 1\rangle$ and $|F=1, m_F=0\rangle$ (Fig. 1a inset(i)) [25]. These couplings correspond to the weak drives $\eta_{-1,0}$, $\eta_{0,1}$ [17]. When the control fields are adiabatically switched off at t_{II} , the probe gets stored as two dark state polaritons (DSPs) [26–32], in atomic coherences $\rho_{-1,0}$ and $\rho_{0,1}$. In the dark (during t_{III}), the coherences (generated due to classical control and probe fields) evolve freely, acquiring relative dynamic phase corresponding to an applied magnetic field. When the excitations are retrieved back as optical field (by turning on control fields $\Omega_{c(R)}^\pm$ at t_{IV}), this dynamic phase difference results in interference fringes. If the weak drives are out of phase, numerically reconstructed state of the spin-1 system shows a limit cycle with no sign of phase entrainment. However, when two asymmetric decay rates (γ_d and γ_g) are introduced using two independent circularly polarized fields (Fig. 1a, inset(ii)), the reconstructed state gets localized for all phases. Correspondingly, we observe a lifting of synchronization blockade for increasing asymmetric decay rates and emergence of Arnold tongue like feature with increasing drive. This is our primary observation.

Figure 1d and e show typical experimental time traces for stored and retrieved probe pulse, in absence and presence of applied magnetic field, respectively. Numerically simulated time traces are in excellent agreement with observations (see Supplementary Information). From simulations, we reconstruct the state of the underlying spin-1 atom (corresponding to $|F=1\rangle$ manifold) and visualize its dynamics by plotting the corresponding Husimi-Q function [15] in phase space, parametrized by the angles θ and ϕ . In particular, the azimuthal angle ϕ remains unspecified for the initial limit cycle state

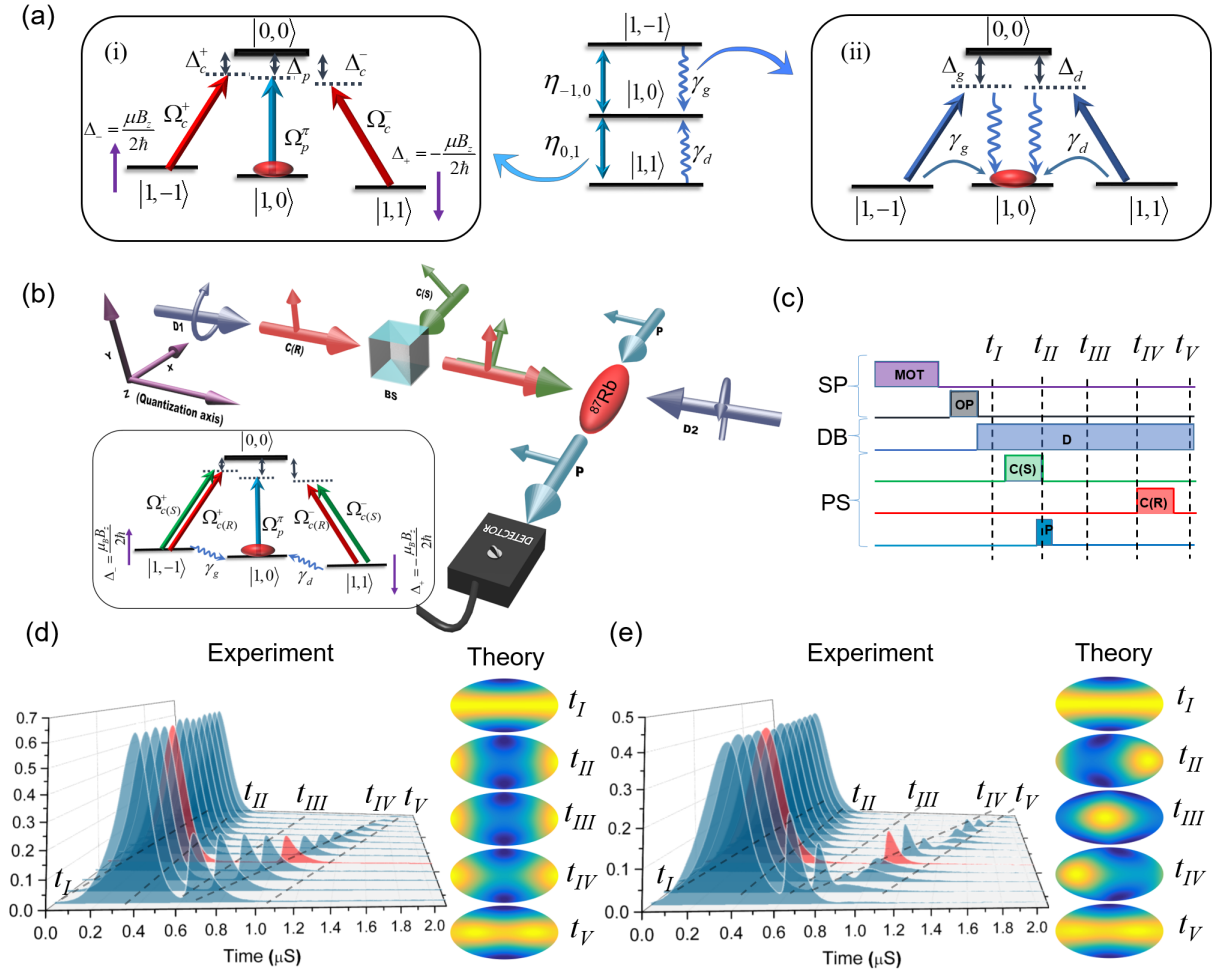


Figure 1. (a) Model of a spin-1 atom with coherent couplings $\eta_{-1,0}$ and $\eta_{0,1}$ along with *incoherent* decay rates γ_g and γ_d . (a.i) The coherent couplings are engineered with two-photon coupling using circularly polarized control fields (Ω_c^\pm) and a π probe field Ω_p^π . (a.ii) Decay rates γ_g and γ_d are engineered with two circularly polarized fields coupling the states $|1, -1\rangle$ and $|1, 1\rangle$ to the excited state $|0, 0\rangle$, such that they are counter-propagating, detuned and phase mismatched. (b) Schematic of experimental setup, showing directions of the linearly polarized storing and retrieving control fields, $C(S)$ and $C(R)$, respectively; a π -polarized probe field in direction perpendicular to the quantization axis and circularly polarized, counter propagating decays beams at small angles to control fields. (c) Timing sequence of the experiment, where SP, DB, and PS correspond to time intervals for state preparation, decay beams and DSP experiments, respectively (see Supplementary Information). (d) Time trace of stored and retrieved probe pulse with varying storage times, with $\phi_c = \Delta = 0$. The corresponding numerically simulated Husimi-Q functions are plotted at different time instances. (e) In presence of magnetic field resulting in a dynamic phase $\Delta = 1.34$ MHz (the tone phase set to zero), the retrieved pulse intensity show fringes due to the dynamic phase difference of the stored DSPs. Phase space plots show a localized spin-1 state, generated at the instance of storage and precessing in the equatorial plane entrained with the dynamic phase.

$|F = 1, m_F = 0\rangle$ [15, 17]. However, when the two control fields are in phase along with the probe field, it is illuminating to note that the corresponding spin-1 atomic state gets localized in phase space (see ‘‘Theory’’ plots, Fig. 1d and e). In particular, in presence of a finite magnetic field (Δ), this localized state is entrained with the dynamic phase and to the classical (or tone) phase difference, ϕ_c , of the two control fields. The resulting reconstructed state (Fig. 1e), precess freely in the equatorial plane acquiring a dynamic phase difference $2\Delta\tau = \mu_B B_z \tau / \hbar$. This phase results in fringes in the retrieved pulse inten-

sity along the probe direction (Fig. 1e). However, when the control fields are out of phase ($\phi_c = \pi$) interfering destructively, the state remains delocalized as a distorted limit cycle (Fig. 2).

Figure 2a shows typical experimental plot of the retrieved intensity, $I_R(\tau)$ at $\tau = 600$ ns, as a function of tone (ϕ_c) and dynamic (Δ) phases. The tone phase is varied by varying the difference of the difference phases between the storing ($\Omega_{c(S)}^\pm$) and retrieving ($\Omega_{c(R)}^\pm$) control fields. The dynamic phase is changed by applying a magnetic field along the quantization axis (z ,

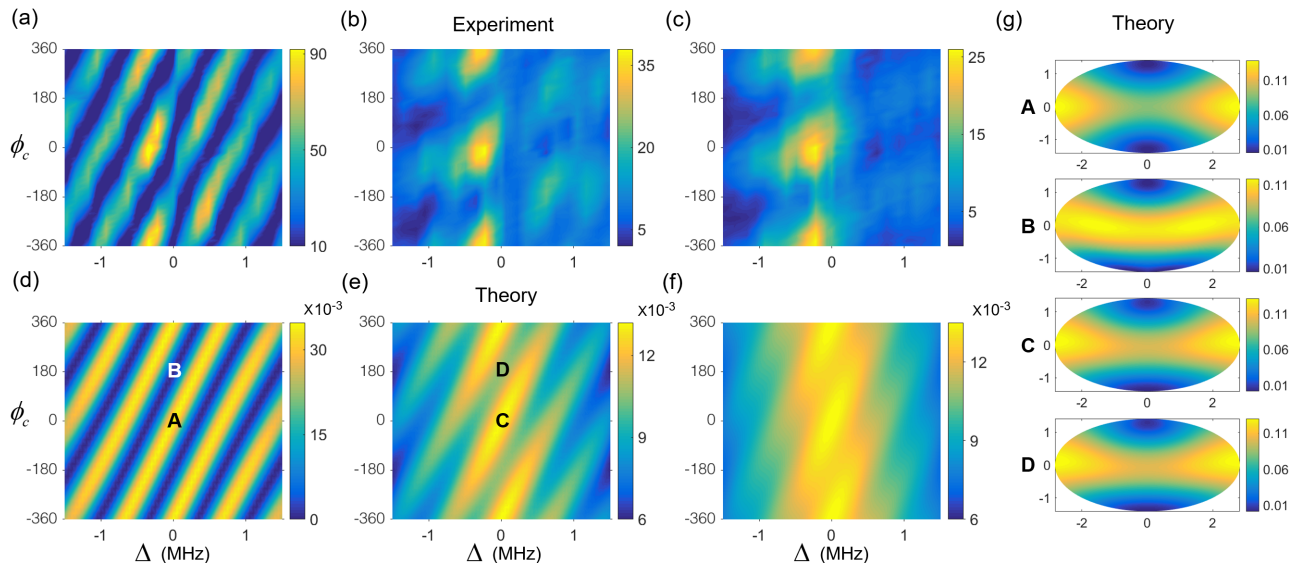


Figure 2. (a-c) Plot of retrieved intensity as a function of dynamic (Δ) and tone phase ϕ_c for decay rate ratios: $\gamma_d/\gamma_g = 1.00$ (a), 7.56 (b) and 11.90 (c). (d-f) Numerically simulated plots of retrieved intensity for decay rate ratios: $\gamma_d/\gamma_g = 1.00$ (d), 7.50 (e) and 11.00 (f). (g) Shows the Husimi-Q plots for the regions A, B, C, and D in **d** and **e**, with the x-axis and y-axis being representations of ϕ and θ , respectively. Here the experimental parameters Ω_p^π , $\Omega_{c(S)}^{\text{lin}}$ and $\Omega_{c(R)}^{\text{lin}}$ are set to 0.64γ , 1.02γ and 1.44γ , respectively and $\gamma_g = 107$ kHz, and the simulation parameters are as tabulated in Supplementary Information. Colour bars for experimental plots are in units of $\mu\text{W}/\text{cm}^2$ and for theory plots, in units of $2|\Omega_R|^2/\gamma^2$, where $|\Omega_R|$ and γ correspond retrieved field and excited state decay, respectively. For (g), the colour bar corresponds to magnitudes of Husimi-Q function.

Fig. 1b). Experimentally, we observe sinusoidally varying fringes with both phases, when γ_g and γ_d are kept equal. This is in agreement with a model of two interfering DSPs, with the retrieved pulse intensity: $I_R(\tau) \propto |\Omega_{c(R)}|^2 e^{-\tau^2/2\tau_D^2} \cos^2 \frac{1}{2}(\phi_c + 2\Delta\tau)$, where τ_D is the DSP decoherence time-scale (see Supplementary Information). However, as the decay rates are made anisotropic, there is a decrease in visibility and the retrieved signal intensity varies with the tone phase i.e. ϕ_c (Fig. 2b and c). Numerical simulations with comparable parameters are in general agreement with observations (Fig. 2e and f).

From reconstructed states, we observe that when the DSPs interfere constructively, the spin-1 state is localized in phase space (region A, Fig. 2d and g). On the contrary, when the DSPs destructively interfere the state remains delocalized, with no synchronization (region B, Fig. 2d and g). Nevertheless, in presence of anisotropic decays, the state gets localized and synchronized, for both constructive and destructive interferences (regions C and D, Fig. 2e and g). This is the primary signature of synchronization of the spin-1 state in phase space.

In particular, at regions of destructive interference of DSPs, there is a rich interplay between quantum coherence and classical decay rates. When the rates are asymmetric and smaller than Δ , destructive interference between generated coherences leads to a null in the retrieved pulse. However, when the larger of the rates, γ_d , gets comparable to Δ , the coherences interfere only partially, resulting in emergence of synchronization. Figure 3

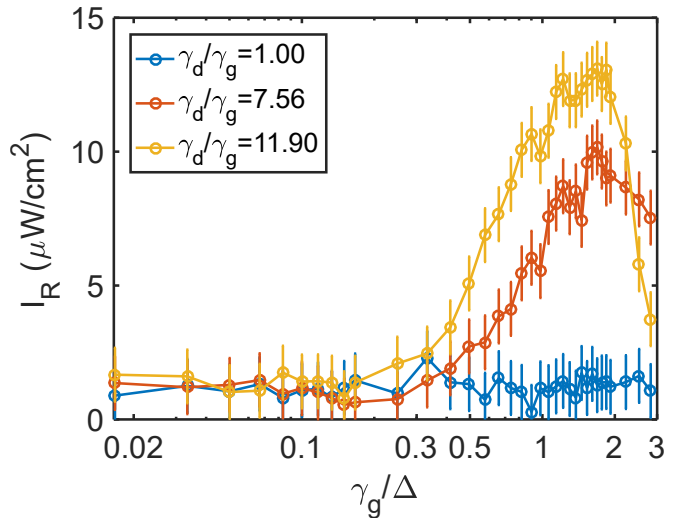


Figure 3. Retrieved intensity for destructive interference is plotted as a function of increasing γ_g , for a fixed dynamic phase Δ . Symmetric decay rates correspond to blue curve while asymmetric decay rates are represented with yellow and red. Here the experimental parameters Ω_p^π , $\Omega_{c(S)}^{\text{lin}}$ and $\Omega_{c(R)}^{\text{lin}}$ are set to 0.64γ , 1.02γ and 1.44γ , $\phi_c = 140^\circ$ and dynamic phase $\Delta = 67$ kHz, corresponding to a fixed magnetic field.

depicts an extended region ($\gamma_d < \Delta$) where destructive interference results in no synchronization and in negligible retrieved pulse intensity. However, as the decay rates are made asymmetric and with $\gamma_d > \Delta$, we again retrieve

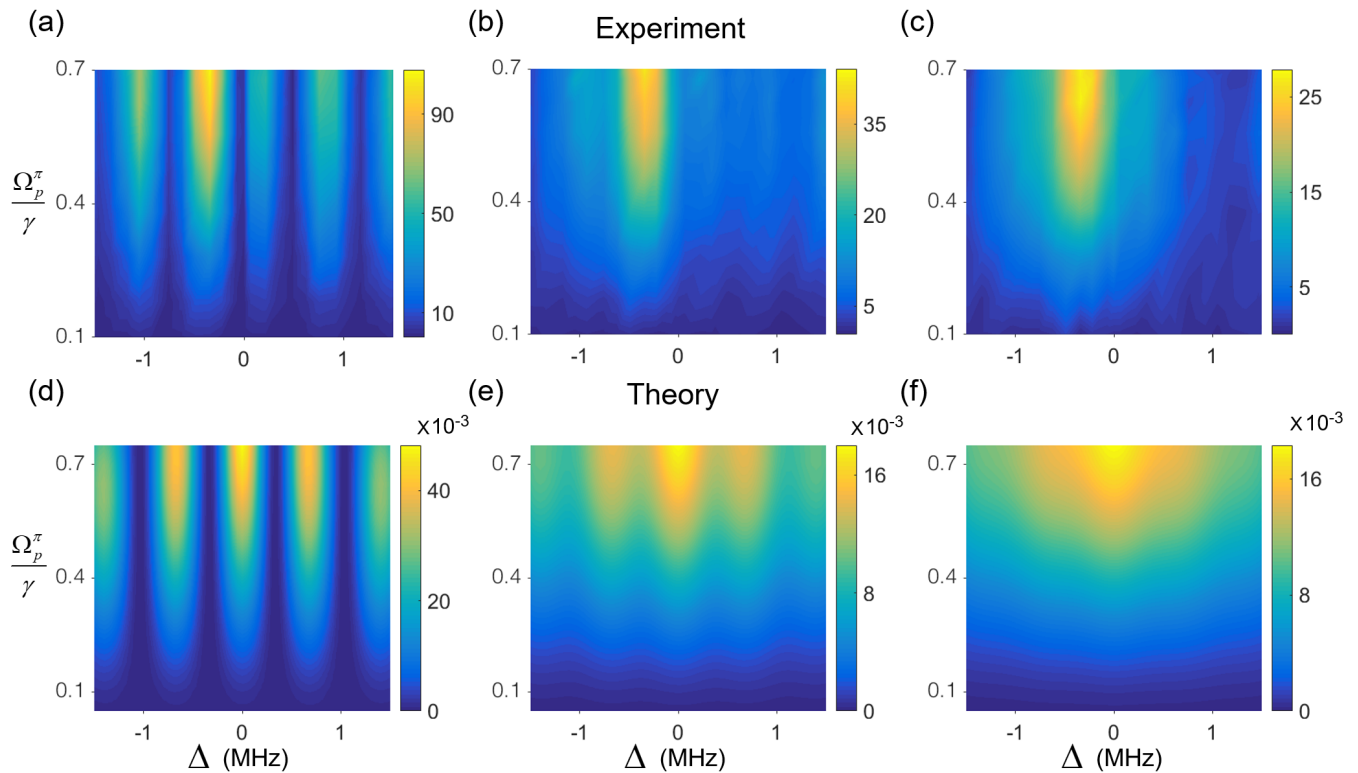


Figure 4. (a-c) Retrieved intensity is plotted with probe field strength (Ω_p^π) and dynamic phase (Δ), for symmetric (a) and asymmetric (b and c) decay rates. The asymmetric decay ratios are $\gamma_d/\gamma_g = 7.56$ for (b) and 11.90 for (c), respectively. (d-f) Corresponding simulated plots for decay ratios 1.00 (d), 7.50 (e) and 11.00 (f). Here experimental parameters $\Omega_{c(S)}^{\text{lin}}$ and $\Omega_{c(R)}^{\text{lin}}$ are set to 1.02γ and 1.44γ , respectively and $\gamma_g = 107$ kHz and simulation parameters are as tabulated in Supplementary Information. Colour bars for experimental plots are in units of $\mu\text{W}/\text{cm}^2$ and for theory plots, in units of $2|\Omega_R|^2/\gamma^2$.

a signal. Such *synchronization blockade* due to quantum interference and decay induced phase locking has been predicted as signature for genuine quantum synchronization [13, 15]. When both decay rates are large, we observe an overall decrease in retrieved intensity.

Furthermore, we observe emergence of Arnold tongue-like features in retrieved pulse intensity, with increasing field strength Ω_p^π and changing magnetic field (Fig. 4). When the two decay rates γ_g and γ_d are equal (Fig. 4a and d), we observe distinct fringes due to changing dynamic phase, along with monotonic increase of the retrieved signal with increasing probe field strength Ω_p^π . As the decay rates are made unequal, with $\gamma_d > \gamma_g$ (Fig. 4b, c, e and f), the central maxima eventually broadens with increasing Ω_p^π into a typical Arnold-tongue like shape. Numerical simulations are in general agreement with observations.

To conclude, coherence has been predicted as a key resource to observe quantum synchronization [17]. Here we use techniques from stored light to generate, evolve and retrieve coherences [25, 33] as polaritons in spin-1 atoms. In particular, we observe that anisotropic decays induce synchronization or entrain the relative dynamic phase of two polaritons. Synchronization of multiple such

polaritons can lead to collective states of fundamental interests [34] and as synchronized quantum memories for quantum technologies.

We thank Sourin Das, Sagar Chakraborty, Harshwardhan Wanare, Umakant Rapol and Anurag Gupta for insightful discussions and comments on the work. SV acknowledges support from the DST-SERB Early Career Research Award (ECR/2018/000957) and discussions with M.Hajdušek. PA acknowledges financial support from UGC. SM acknowledges financial support from CSIR. This work was supported under SERB-DST grant no: SERB/PHY/2015404.

* gsaiikat@iitk.ac.in

- [1] S. Strogatz, *Sync: The Emerging Science of Spontaneous Order (Penguin Press Science)* (Penguin Books, Limited (UK), 2008).
- [2] W. Lewandowski and E. F. Arias, *Metrologia* **48**, S219 (2011).
- [3] M. Rohden, A. Sorge, M. Timme, and D. Witthaut, *Phys. Rev. Lett.* **109**, 064101 (2012).
- [4] J.-D. Deschênes, L. C. Sinclair, F. R. Giorgetta, W. C. Swann, E. Baumann, H. Bergeron, M. Cermak, I. Cod-

- dington, and N. R. Newbury, Phys. Rev. X **6**, 021016 (2016).
- [5] J. Cidras, A. E. Feijoo, and C. Carrillo Gonzalez, IEEE Transactions on Power Systems **17**, 1162 (2002).
- [6] H. J. Kimble, Nature **453**, 1023 (2008).
- [7] G. Manzano, F. Galve, G. L. Giorgi, E. Hernández-García, and R. Zambrini, Scientific Reports **3** (2013).
- [8] A. Mari, A. Farace, N. Didier, V. Giovannetti, and R. Fazio, Phys. Rev. Lett. **111**, 103605 (2013).
- [9] S. Walter, A. Nunnenkamp, and C. Bruder, Phys. Rev. Lett. **112**, 094102 (2014).
- [10] T. E. Lee, C.-K. Chan, and S. Wang, Phys. Rev. E **89**, 022913 (2014).
- [11] N. Lörch, E. Amitai, A. Nunnenkamp, and C. Bruder, Phys. Rev. Lett. **117**, 073601 (2016).
- [12] T. Weiss, S. Walter, and F. Marquardt, Phys. Rev. A **95**, 041802 (2017).
- [13] N. Lörch, S. E. Nigg, A. Nunnenkamp, R. P. Tiwari, and C. Bruder, Phys. Rev. Lett. **118**, 243602 (2017).
- [14] T. Weiß, *Nonlinear dynamics in quantum synchronization and topological transport*, Ph.D. thesis, Naturwissenschaftliche Fakultät (2017).
- [15] A. Roulet and C. Bruder, Phys. Rev. Lett. **121**, 053601 (2018).
- [16] S. Sonar, M. Hajdušek, M. Mukherjee, R. Fazio, V. Vedral, S. Vinjanampathy, and L.-C. Kwek, Phys. Rev. Lett. **120**, 163601 (2018).
- [17] M. Koppenhöfer and A. Roulet, Phys. Rev. A **99**, 043804 (2019).
- [18] A. Roulet and C. Bruder, Phys. Rev. Lett. **121**, 063601 (2018).
- [19] L.-M. Duan, M. D. Lukin, J. I. Cirac, and P. Zoller, Nature **414**, 413 (2001).
- [20] T. E. Lee and H. R. Sadeghpour, Phys. Rev. Lett. **111**, 234101 (2013).
- [21] D. Witthaut, S. Wimberger, R. Burioni, and M. Timme, Nature Communications **8** (2017).
- [22] V. M. Bastidas, I. Omelchenko, A. Zakharova, E. Schöll, and T. Brandes, Phys. Rev. E **92**, 062924 (2015).
- [23] A. Cabot, G. L. Giorgi, F. Galve, and R. Zambrini, Phys. Rev. Lett. **123**, 023604 (2019).
- [24] Y. Lee Loh and M. Kim, American Journal of Physics **83**, 30 (2015).
- [25] A. W. Laskar, N. Singh, P. Adhikary, A. Mukherjee, and S. Ghosh, Optica **5**, 1462 (2018).
- [26] M. D. Lukin, S. F. Yelin, and M. Fleischhauer, Phys. Rev. Lett. **84**, 4232 (2000).
- [27] C. Liu, Z. Dutton, C. H. Behroozi, and L. V. Hau, Nature **409**, 490 (2001).
- [28] D. F. Phillips, A. Fleischhauer, A. Mair, R. L. Walsworth, and M. D. Lukin, Phys. Rev. Lett. **86**, 783 (2001).
- [29] M. Fleischhauer and M. D. Lukin, Phys. Rev. A **65**, 022314 (2002).
- [30] L. Karpa, F. Vewinger, and M. Weitz, Phys. Rev. Lett. **101**, 170406 (2008).
- [31] H. Wang, S. Li, Z. Xu, X. Zhao, L. Zhang, J. Li, Y. Wu, C. Xie, K. Peng, and M. Xiao, Phys. Rev. A **83**, 043815 (2011).
- [32] Y. O. Dudin, L. Li, and A. Kuzmich, Phys. Rev. A **87**, 031801 (2013).
- [33] A. W. Laskar, N. Singh, A. Mukherjee, and S. Ghosh, New Journal of Physics **18**, 053022 (2016).
- [34] R. H. Dicke, Phys. Rev. **93**, 99 (1954).

Supplementary information:

Here, we provide details of the numerical simulations used to reconstruct the spin-1 states and discuss construction of the Husimi-Q function for visualization of the state in phase space. We provide an analytic model describing interferometry of dark-state-polaritons (DSPs) and how the resulting signal bears signature of quantum synchronization. We also document some experimental details pertaining to the experiment and measurements presented here.

S.I. Methods

Experiment:

Atomic system: ^{87}Rb atoms are laser-cooled and trapped in a cigar-shaped cloud at a temperature of $\sim 121\mu\text{K}$. After turning off all cooling and trapping fields, the atoms are pumped to the state $|F=1, m_F=0\rangle$ using a pair of optical fields by first placing the atoms in $F=1$ ground state manifold and then spin polarizing them to the particular state.

Couplings: Two kinds of couplings are engineered for the experiment-*coherent* two-photon couplings and *incoherent* decay rates between states. For *coherent* couplings, a linearly polarized laser ($\Omega_{c(S)}^{\text{lin}}$), composed of two circularly polarized control fields ($\Omega_{c(S)}^{\pm}$), is used to store a π -polarized probe field (Ω_p^{π}). At a later time, a second linearly polarized laser ($\Omega_{c(R)}^{\text{lin}}$), composed of two circularly polarized fields ($\Omega_{c(R)}^{\pm}$), is turned on to retrieve the stored excitation from the atomic medium. The control and the probe laser fields are all locked on resonance to the transition ($|F=1\rangle \rightarrow |F'=0\rangle$).

The *incoherent* couplings or decay rates (γ_g and γ_d) are engineered using two independent circularly polarized lasers fields that are tuned to transitions $|F=1, m_F=\pm 1\rangle \rightarrow |F'=0, m_{F'}=0\rangle$. These decay beams are kept at a constant red-detuning of 4 MHz red from this transition, even in presence of magnetic field, by driving their corresponding acousto-optic-modulators (AOMS) with independent frequency sources. This process ensures that the decay rates and their ratios remain constant as the magnetic field is varied along the quantization axis. Furthermore, the decay beams are counter-propagating to each other and are deliberately maintained at a small angle with respect to the control fields to ensure minimal coherence induced by these decay fields in the system.

Phases: The *tone phase*, ϕ_c , is the difference of the phase difference, $\phi_S - \phi_R$, between the storing ($\Omega_{c(S)}^{\pm}$) and retrieved $\Omega_{c(R)}^{\pm}$ control fields. The tone phase is varied by varying the linear polarization of the storing field with respect to the retrieving control fields. The *dynamic phase* is varied by applying a magnetic field along the quantization axis with a pair of coils in Helmholtz configuration.

Lasers and experimental cycle: All lasers are frequency locked either to atomic transitions or to frequency stabilized sources using beat-note techniques. VCOs are used for to tune the laser frequency dynamically while AOMs are used to create pulses or for turning fields on and off. In particular, the probe pulse width is set at ~ 250 ns and the control field rise and fall ramp time at ~ 100 ns. Amplitude, frequency and timing of lasers and magnetic fields are computer controlled, using a combination of NI-DAQ system (PXIe-6738) and FPGA (XEM3001) for slow and fast timing control, respectively.

S.II. Numerical simulations:

We numerically solve optical Bloch equations and simulate time dynamics of the probe pulse in presence and absence of a control field. We observe numerically simulated probe transmission traces to be in excellent agreement with experiments (Fig. 5). We use this correspondence to reconstruct the density matrix of experimental spin-1 atoms and plot the corresponding state projection (Husimi-Q function) in phase space.

(a) Optical Bloch equations and density matrix elements:

To simulate our experiment, we construct a 4-level atomic system with three ground states $|1\rangle, |2\rangle, |3\rangle$ and an excited state $|4\rangle$. These ground and excited states correspond to $|F=1, m_F=-1\rangle, |F=1, m_F=0\rangle, |F=1, m_F=1\rangle$ hyperfine ground states and $|F'=0, m_{F'}=0\rangle$ excited states, corresponding to D2 transition of ^{87}Rb atoms. We denote them as, $|1\rangle \equiv |F=1, m_F=-1\rangle, |2\rangle \equiv |F=1, m_F=0\rangle, |3\rangle \equiv |F=1, m_F=1\rangle$, and $|4\rangle \equiv |F'=0, m_{F'}=0\rangle$ and we consider the atoms to be independent entities.

The effective Hamiltonian of such a four-level system can be expressed, in a rotating frame, as:

$$\hat{H} = -\hbar \begin{bmatrix} (\Delta_p - \Delta_c^+ + \Delta) & 0 & 0 & \Omega_c'^+ \\ 0 & 0 & 0 & \Omega_p' \\ 0 & 0 & (\Delta_p - \Delta_c^- - \Delta) & \Omega_c'^- \\ (\Omega_c'^+)^* & \Omega_p'^* & (\Omega_c'^-)^* & \Delta_p \end{bmatrix}. \quad (1)$$

Here the control Rabi frequency at different times are defined as:

$$\Omega_c^{\pm}(z, t) = \begin{cases} \Omega_{c(S)}^{\pm}(z, 0)e^{-(t-t_{on})^2/2\tau_c^2}e^{i\phi_S^{\pm}} & \text{if } t \leq t_{on1} \\ \Omega_{c(S)}^{\pm}(z, 0)e^{i\phi_S^{\pm}} & \text{if } t_{on1} < t \leq t_{off} \\ \Omega_{c(S)}^{\pm}(z, 0)e^{-(t-t_{off})^2/2\tau_c^2}e^{i\phi_S^{\pm}} + \Omega_{c(R)}^{\pm}(z, 0)e^{-(t-t_{on2})^2/2\tau_c^2} & \text{if } t_{off} < t \leq t_{on2} \\ \Omega_{c(R)}^{\pm}(z, 0) & \text{if } t > t_{on2} \end{cases}, \quad (2)$$

where $\tau_c = 70$ ns is the ramp time corresponding to turn on and off of the storing (retrieving) control fields, $\Omega_{c(S)}^+$ ($\Omega_{c(R)}^+$) and $\Omega_{c(S)}^-$ ($\Omega_{c(R)}^-$), connect the levels $|1\rangle$ and $|3\rangle$ to $|4\rangle$, respectively (Fig. 1, main text). The difference of the two control field phases, $\phi_c = \phi_S^+ - \phi_S^-$, is what we refer to in main text as the tone phase. The phase difference of the coherences of the spin-1 atoms i.e. the phase difference between the two DSPs locks to this classical tone phase when synchronized in presence of anisotropic decay.

At time instance t_{on1} , when the control fields ($\Omega_{c(S)}^{\pm}$) are (adiabatically) turned on and in presence of a probe pulse, two DSPs form in the system. A part of the DSPs is electromagnetic field dependent while the other part is atomic coherence. When the control fields are (adiabatically) turned off at time instance t_{off} , the DSPs are purely atomic and get stored in the form of ground state coherences (ρ_{12} and ρ_{23}). This stored excitations are converted back into electromagnetic fields, when the control fields with Rabi frequencies $\Omega_{c(R)}^{\pm}(z, 0) = f\Omega_{c(S)}^{\pm}(z, 0)$, amplified by a factor f , are turned back on at time instance t_{on2} . The corresponding two atomic coherences, when mapped back photonic state, interfere and the phase of interference varies with either varying dynamics phase (by applied magnetic field) or with varying tone phase i.e. the difference of the phase the two circularly polarized control fields. Experimentally, we change the tone phase using a half wave plate in the path of the control fields.

Numerically, we set the turn on and turn off times for control fields at $t_{on1} = 0.4 \mu\text{s}$, $t_{off} = 1.91 \mu\text{s}$, while the storage time is varied by varying t_{on2} for the following experiments (Fig. 5). The probe Rabi frequency is defined as

$$\Omega_p'(z, t) = \Omega_p'(z, 0)e^{-(t-t_p)^2/2\tau_p^2} \forall t \quad (3)$$

We turn on the probe pulse at $t_p = 1.90 \mu\text{s}$. It has a pulse width $\tau_p = 200$ ns. The probe field connects $|2\rangle \rightarrow |4\rangle$ transition. The Rabi frequencies of the control fields are defined as $\Omega_{c,p}^{\pm} = d_{c,p}^{\pm} \cdot \mathcal{E}_{c,p}^{\pm}/\hbar = 2\Omega_{c,p}'$, where $d_{c,p}^{\pm}$ correspond to the transition dipole moment, and $\mathcal{E}_{c,p}^{\pm}$ electric field amplitude for the corresponding fields. The detuning of the fields from atomic transition energies are $\Delta_c^+ = \omega_c^+ - \omega_{14}$, $\Delta_c^- = \omega_c^- - \omega_{34}$, and $\Delta_p = \omega_p - \omega_{24}$. Here ω_c^+ , ω_c^- , and ω_p correspond to respective laser frequencies. To incorporate effect of the applied magnetic field (along the quantization axis), we add energy shifts Δ_- and Δ_+ to the ground state energies of $|1\rangle$ and $|3\rangle$, respectively (Fig. 1a, inset(i)). Here $\Delta_+ = -\Delta_- = \Delta$.

Dynamics of the atomic density matrix of the the 4-level atom is governed by a master equation which can be expressed as:

$$\dot{\hat{\rho}}(t) = -\frac{i}{\hbar}[\hat{H}, \hat{\rho}] + \hat{\mathcal{L}}(\hat{\rho}). \quad (4)$$

where H stands for the system Hamiltonian (eqn. (1)), and $\hat{\mathcal{L}}(\hat{\rho})$ includes all the decays. We numerically integrate the master equation (4). The corresponding dynamical equations for elements of the density matrix are:

$$\dot{\rho}_{11} = -i[\rho_{14}^*(\Omega_c^+)^* - \rho_{14}\Omega_c^+] + \Gamma_{41}\rho_{44} - \gamma_g\rho_{11} - \gamma_{th}(\rho_{11} - \rho_{11}^{eq}) \quad (5)$$

$$\dot{\rho}_{12} = -i[\rho_{12}(\Delta_p - \Delta_c^+ + \Delta) + \rho_{24}^*(\Omega_c^+)^* - \rho_{14}\Omega_p'] - (\gamma_{12} + \gamma_{th})\rho_{12} \quad (6)$$

$$\dot{\rho}_{13} = -i[\rho_{13}(\Delta_c^- - \Delta_c^+ + 2\Delta) + \rho_{34}^*(\Omega_c^+)^* - \rho_{14}\Omega_c'^-] - (\gamma_{13} + \gamma_{th})\rho_{13} \quad (7)$$

$$\dot{\rho}_{14} = -i[(\Omega_c^+)^*(\rho_{44} - \rho_{11}) - \rho_{12}\Omega_p'^* + \Delta\rho_{14} - \rho_{13}(\Omega_c'^-)^* - \Delta_c^+\rho_{14}] - (\gamma_{41} + \gamma_{th})\rho_{14} \quad (8)$$

$$\dot{\rho}_{22} = -i[\rho_{24}^*\Omega_p'^* - \rho_{24}\Omega_p'] + \Gamma_{42}\rho_{44} + \gamma_g\rho_{11} + \gamma_d\rho_{33} - \gamma_{th}(\rho_{22} - \rho_{22}^{eq}) \quad (9)$$

$$\dot{\rho}_{23} = -i[\rho_{23}(\Delta_c^- - \Delta_p + \Delta) + \rho_{34}^*\Omega_p'^* - \rho_{24}\Omega_c'^-] - (\gamma_{23} + \gamma_{th})\rho_{23} \quad (10)$$

$$\dot{\rho}_{24} = -i[\Omega_p'^*(\rho_{44} - \rho_{22}) - \rho_{23}(\Omega_c'^-)^* - \rho_{12}^*(\Omega_c^+)^* - \Delta_p\rho_{24}] - (\gamma_{42} + \gamma_{th})\rho_{24} \quad (11)$$

$$\dot{\rho}_{33} = -i[\rho_{34}^*(\Omega_c'^-)^* - \rho_{34}\Omega_c'^-] + \Gamma_{43}\rho_{44} - \gamma_d\rho_{33} - \gamma_{th}(\rho_{33} - \rho_{33}^{eq}) \quad (12)$$

$$\dot{\rho}_{34} = -i[(\Omega_c'^-)^*(\rho_{44} - \rho_{33}) - \rho_{13}^*(\Omega_c^+)^* - \rho_{23}^*\Omega_p'^* - \Delta\rho_{34} - \Delta_c^-\rho_{34}] - (\gamma_{43} + \gamma_{th})\rho_{34} \quad (13)$$

$$\begin{aligned} \dot{\rho}_{44} = & -i[-\rho_{34}^*(\Omega_c'^-)^* + \rho_{34}\Omega_c'^- - \rho_{14}^*(\Omega_c^+)^* + \rho_{14}\Omega_c^+ - \rho_{24}^*\Omega_p'^* + \rho_{24}\Omega_p'] \\ & - \Gamma_{44}\rho_{44} - \gamma_{th}(\rho_{44} - \rho_{44}^{eq}). \end{aligned} \quad (14)$$

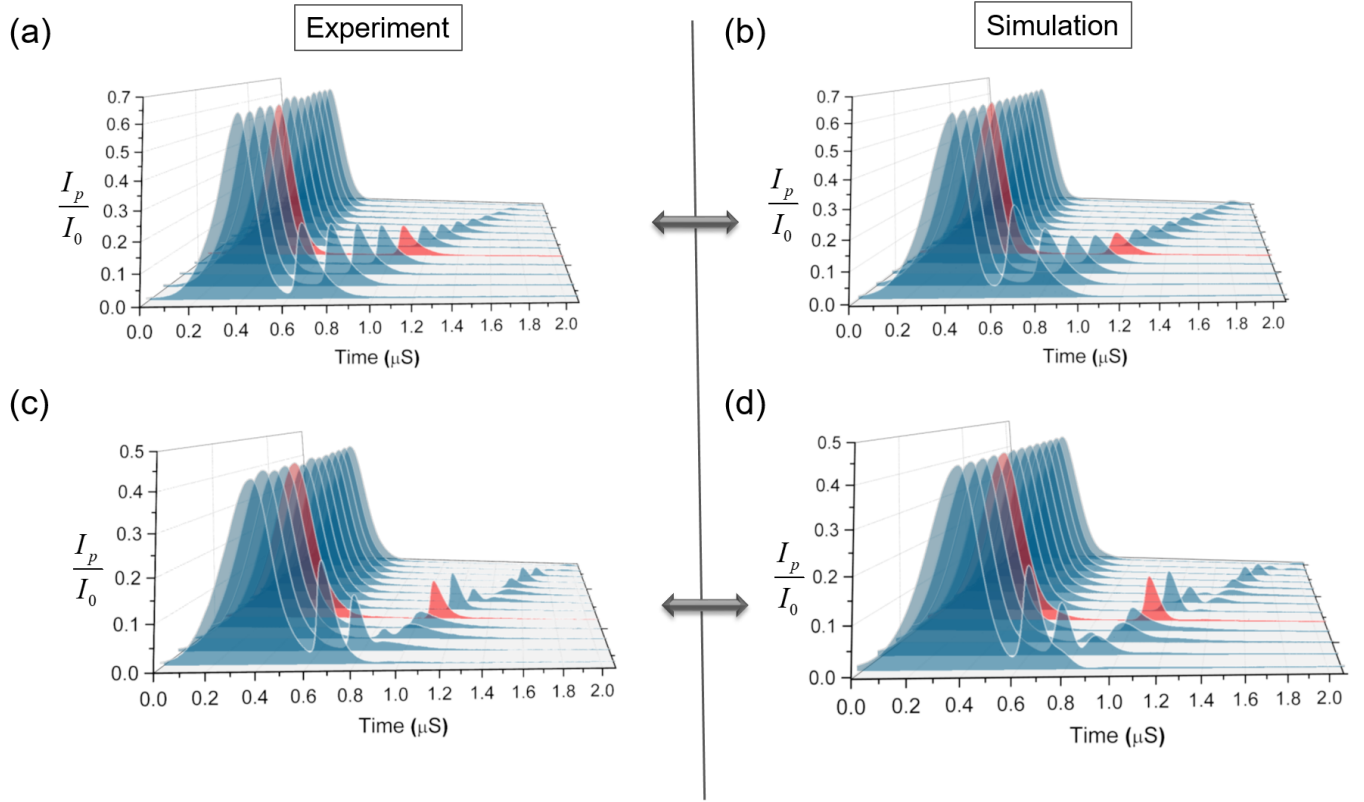


Figure 5. (a) and (c) Experimental plots of stored and retrieved probe pulse with varying storage time τ for zero magnetic field ($\Delta = 0$) and $\Delta = 1.34$ MHz, respectively. (b) and (d) simulated plots of stored and retrieval probe pulse to simulate the probe pulse obtained in experiments corresponding to (a) and (c) with $\Delta = 0$ and 1.05 MHz, respectively. Here I_p and I_0 are transmitted and input probe field intensities. Parameters for simulations are as tabulated in Table S1.

Here Γ_{41}, Γ_{42} , and Γ_{43} are the effective radiative decays from $|4\rangle$ to $|1\rangle, |2\rangle$, and $|3\rangle$, respectively, and are expressed as: $\Gamma_{41} = \Gamma_{42} = \Gamma_{43} = \Gamma_{44}/3$. The rate γ_{th} is used for Doppler decoherence and is taken as thermal transit time of the atoms through the transverse cross-section of the probe beam. γ_g and γ_d correspond to the engineered incoherent decay from $|1\rangle$ and $|3\rangle$ to $|2\rangle$, respectively.

$$\gamma_{12} = \gamma_g/2 + \gamma_{dec} \quad (15)$$

$$\gamma_{13} = \gamma_g/2 + \gamma_d/2 + \gamma_{dec} \quad (16)$$

$$\gamma_{23} = \gamma_d/2 + \gamma_{dec} \quad (17)$$

$$\gamma_{43} = \gamma_d/2 + \Gamma_{44}/2 + \gamma_{dec} \quad (18)$$

$$\gamma_{42} = \Gamma_{44}/2 + \gamma_{dec} \quad (19)$$

$$\gamma_{41} = \Gamma_{44}/2 + \gamma_g/2 + \gamma_{dec}, \quad (20)$$

where γ_{dec} is a decoherence due to other effects including stray, oscillating magnetic fields, vacuum impurity, and wave-vector phase mismatch due to angles between control and probe fields.

We simultaneously and self-consistently integrate the corresponding Maxwell equation to obtain dynamical evolution of the propagating probe field. Using slowly-varying-envelope-approximation (SVEA), the corresponding wave equations for fields can be expressed as:

$$\frac{1}{c} \frac{\partial}{\partial t} \Omega_c'^+(z, t) + \frac{\partial}{\partial z} \Omega_c'^+(z, t) = -i\mu_a \rho_{14}(z, t) \quad (21)$$

$$\frac{1}{c} \frac{\partial}{\partial t} \Omega_c'^-(z, t) + \frac{\partial}{\partial z} \Omega_c'^-(z, t) = -i\mu_a \rho_{34}(z, t) \quad (22)$$

$$\frac{1}{c} \frac{\partial}{\partial t} \Omega_p'(z, t) + \frac{\partial}{\partial z} \Omega_p'(z, t) = -i\mu_a \rho_{24}(z, t). \quad (23)$$

Parameters	Γ_{44}	γ_{th}	γ_{dec}	$ \Omega_{c(S)}^+ $	$ \Omega_{c(S)}^- $	$ \Omega_p $	γ_g	Δ	f
Values	(2π) 6 MHz	(2π) 0.01 MHz	(2π) 0.15 MHz	$0.95 \Gamma_{44}$	$0.95 \Gamma_{44}$	$0.55 \Gamma_{44}$	(2π) 0.20 MHz	(2π) 1.05 MHz	1.25

Table I. Parameters used in numerical simulations.

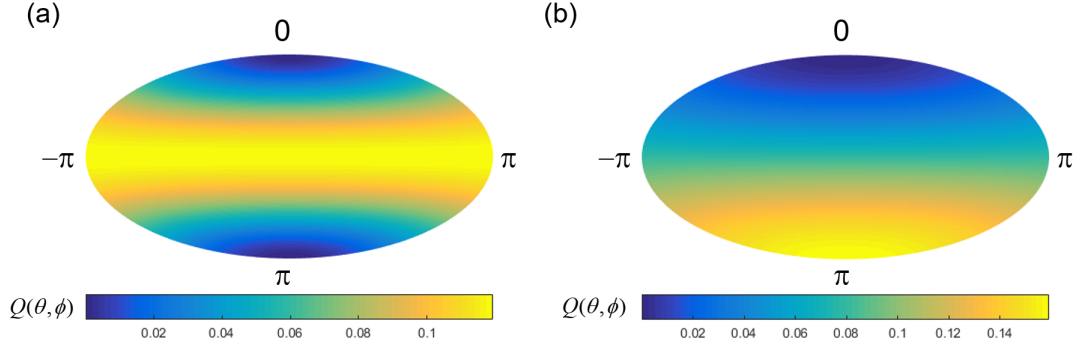


Figure 6. (a) Equatorial limit cycle of spin-1 system with the population in state $|F = 1, m_F = 0\rangle$ or the state $(0,1,0)$. (b) For comparison, a spin-1 state with population $(0, \frac{1}{3}, \frac{2}{3})$ are plotted. This limit cycle resembles a van der Pol oscillator deep in the quantum regime [4, 5].

Here $\mu_a = \frac{Nd^2\omega}{\hbar\epsilon_0}$ where N , d , ω , and ϵ_0 correspond to number of atoms, dipole moment, field frequencies and free space permittivity, respectively. The above equation can further be simplified by introducing the new variables $z = \zeta$ and $t' = t - z/c$ [1]. The wave operator $\partial/\partial z + \partial/\partial ct$ simply takes the form under this transformation as $\partial/\partial \zeta$, and the propagation equation of the fields becomes

$$\frac{\partial}{\partial \zeta} \Omega_c^+(z, t)(\zeta) = -i\mu_a \rho_{14}(\zeta) \quad (24)$$

$$\frac{\partial}{\partial \zeta} \Omega_c^-(z, t)(\zeta) = -i\mu_a \rho_{34}(\zeta) \quad (25)$$

$$\frac{\partial}{\partial \zeta} \Omega_p'(z, t)(\zeta) = -i\mu_a \rho_{24}(\zeta). \quad (26)$$

From the propagation of equation of probe field we obtain the transmitted probe field as $\Omega_p'(\zeta) = \Omega_p'(\zeta - d\zeta) + \int_0^L \alpha \times \text{Im}(\rho_{24}(\zeta))d\zeta$, where L is the length of the medium and α is a constant [2, 3]. Fig. 5a and c show the experimental traces obtained for stored and retrieved probe pulses for varying storage times τ at $\Delta = 0$ and 1.34 MHz, respectively. As we increase the storage time, the retrieved pulse intensity decreases monotonically due to Doppler and other decoherences present in the system. For non zero detuning, an additional dynamic phase $2\Delta\tau$ develops (S.III. Interference of dark state polaritons), and the retrieved pulse intensity develop fringes in time due to the acquired dynamic phase (Fig. 5c). The simulated traces are fitted to experimental traces (Fig. 5) by judiciously choosing and tuning the free parameters in the optical Bloch equations (5)-(14). The simulated traces are not Doppler averaged over the velocity distribution of the atoms. Accordingly, we observe exponential decay of retrieved pulse intensity with increasing storage time. On the contrary, in experiments, we observe Gaussian decay of retrieved pulse and we ascribe the resulting Gaussianity to the essential thermal nature of the ensemble of cold, trapped atoms. The value of the parameters in simulation are listed in Table S1.

(b) Phase space representation (Husimi-Q function) of atomic spin-1 states:

Of the four energy levels that are directly involved in the dynamics, the excited state $|4\rangle = |F' = 0, m_{F'} = 0\rangle$ is short lived with a life time of ~ 30 ns. The corresponding time scales involving probe pulse width and turn on and off times of control fields are significantly longer. Accordingly, most parts of the dynamics can be understood by adiabatically eliminating the excited state and considering the effective spin-1 three-level atom. We use the Husimi-Q function [6] to visualize dynamics of this effective spin-1 atom [7].

Husimi-Q function for a state $\hat{\rho}$ is defined by projecting it in a spin coherent state basis as:

$$Q = \frac{3}{4\pi} \langle \theta, \phi | \hat{\rho} | \theta, \phi \rangle, \quad (27)$$

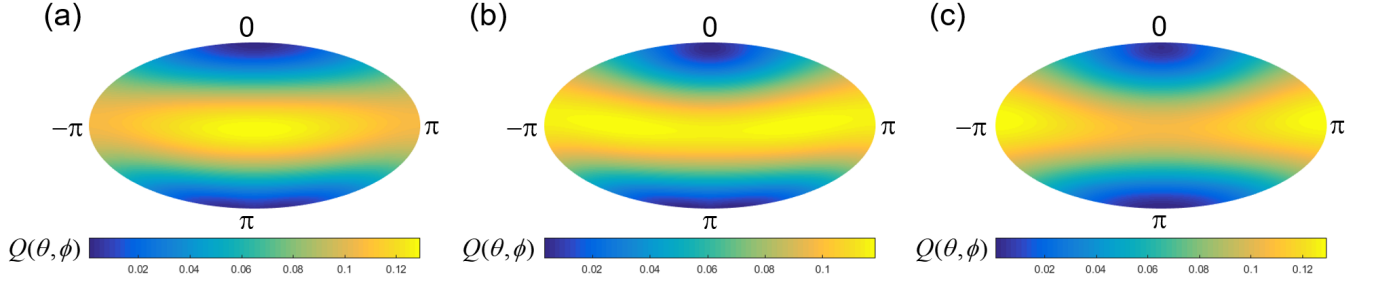


Figure 7. (a) The phase distribution localized around $\phi = 0$ in case of asymmetric decay $\gamma_d/\gamma_g = 0.1$. (b) In the symmetric case $\gamma_d/\gamma_g = 1$ there is no phase localization with slight distortion of the limit cycle. (c) Phase localized state for $\gamma_d/\gamma_g = 10$, localized around $\phi = \pi$.

where $|\theta, \phi\rangle$ is the spin coherent state, and expressed as [8, 9]

$$|\theta, \phi\rangle = \cos^2\frac{\theta}{2} \left(|0\rangle + \sqrt{2}e^{i\phi}\tan\left(\frac{\theta}{2}\right) |1\rangle + e^{i2\phi}\tan^2\left(\frac{\theta}{2}\right) |2\rangle \right). \quad (28)$$

Using the numerically simulated density matrix of the spin-1 three level atom, we plot this function in phase space parametrized by the two angles θ and ϕ .

To establish synchronization, one first needs to establish a limit cycle [7]. Such a limit cycle would be a state with a closed trajectory in phase space. As proposed by Roulet *et. al.*, in presence of anisotropic decays in spin-1 atoms, the limit cycle state gets localized and synchronizes itself to the tone phase at all times.

Limit cycle:

We initialize and prepare an atomic state, which when projected in phase space, forms an equatorial limit cycle corresponding to $\theta = \pi/2$ and precessing about z axis in ϕ . Such a state correspond to all atoms being prepared in state $|F = 1, m_F = 0\rangle$ and its Husimi- Q function is $Q = \frac{3}{4\pi} \langle \theta, \phi | \hat{\rho} | \theta, \phi \rangle = \frac{3}{8\pi} \sin^2\theta$. In Fig. 6b, for comparison, we also plot the Husimi- Q function for a van der Pol limit cycle oscillator deep in quantum regime [10] corresponding to the population $\hat{\rho} = \frac{2}{3} |0\rangle \langle 0| + \frac{1}{3} |1\rangle \langle 1|$.

Synchronization:

For synchronization we first stabilize the equatorial limit cycle state by introducing two decay channels γ_g and γ_d , from states $|1\rangle = |F = 1, m_F = -1\rangle$ and $|3\rangle = |F = 1, m_F = 1\rangle$ to $|2\rangle = |F = 1, m_F = 0\rangle$, respectively. Next we introduce the classical drive with a tone phase, which is the phase difference between the two tones $\eta_{-1,0}$ and $\eta_{0,1}$. The corresponding couplings are stimulated with two photon transitions via an additional level $|4\rangle = |F' = 0, m_{F'} = 0\rangle$, using control fields Ω_c^\pm and a probe Ω_p^π (Fig. 1, main text). When the control field adiabatically turned off, the probe pulse gets stored as DSPs. The storage of the probe pulse with two control fields effectively drives the spin-1 system and creates off-diagonal elements of the density matrix as DSPs.

Simulated Husimi- Q functions for evolving times, calculated from the density matrix elements obtained by solving optical Bloch equations, is plotted in Fig. 7 using Hammer projection of a sphere [11]. At the instance of storage, the limit cycle transforms to a phase localized state with two DSPs constructively interfere corresponding to the tone phase $\phi_c = 0$. This is particularly observable at finite detuning (magnetic field), such that, the phase localized state precess around z -axis with time. This precession leads to interference fringes in retrieved probe intensity at later times. However, when the two DSPs destructively interfere (for $\phi_c = \pi$), the initial limit cycle is only mildly perturbed with the Q function uniformly distributed in the equatorial plane with no signs of phase synchronization (Fig. 7b). The scenario drastically alters when the two decay rates, γ_g and γ_d are made unequal. In such cases, the spin-1 atomic state, at the instance of storage, gets phase localized at $\phi = 0$ and $\phi = \pi$ corresponding to asymmetries $\gamma_d/\gamma_g = 0.1$ (Fig. 7a) or 10 (Fig. 7c), respectively. Most importantly, even in presence of detuning the state remains locked to the tone and dynamic phase, over a certain range of dynamic phase.

S.III. Interference of dark state polaritons (DSPs): derivation of retrieved probe intensity

Here we derive an analytic expression for the retrieved probe pulse intensity in a 4-level atomic system with three ground states. The derived expression for the retrieved probe intensity forms our primary basis for interpreting the experimental data of Figs. 2 and 4 in main text.

Interference of DSPs:

Dark state polaritons are quasiparticles composed of a mixture of atomic and photonic excitations and generated in the phenomenon of electro-magnetically induced transparency (EIT) [12–16]. The corresponding hybrid state propagates through the medium in a shape preserving manner and can be expressed as:

$$\hat{\psi}(z, t) = \cos \theta(t) \hat{E}_p(z, t) - \sin \theta(t) \sqrt{N} \hat{\sigma}_{12}(z, t), \quad (29)$$

$$\cos \theta(t) = \frac{\Omega_c(t)}{\sqrt{|\Omega_c(t)|^2 + g^2 N}}, \quad \sin \theta(t) = \frac{g\sqrt{N}}{\sqrt{|\Omega_c(t)|^2 + g^2 N}}. \quad (30)$$

The state $\hat{\psi}(z, t)$ in turn is governed by the equation of motion [12]:

$$\left[\frac{\partial}{\partial t} + c \cos^2 \theta(t) \frac{\partial}{\partial z} \right] \hat{\psi}(z, t) = 0, \quad (31)$$

where g is the single atom cooperativity and N is the total number of atoms. The generated DSP propagates with a group velocity $v_g(t) = c \cos^2 \theta(t)$, with a possibility of controlling its velocity by adiabatically changing the control Rabi frequency Ω_c . In particular, when the control intensity is turned off, the probe pulse gets stored as superposition of atomic ground states or as atomic coherence. The atomic coherence evolves with time in the presence of a magnetic field, picking up a dynamic phase. One can retrieve the stored excitation back as a probe pulse, by adiabatically turning on the control field at a later time.

We have extended this scheme to include two control fields and three ground states. A similar storage experiment results in two DSPs with relative phase difference between them. In particular, we use two circularly polarized control fields to couple the two edge states $|F = 1, m_F = -1\rangle$ and $|F = 1, m_F = 1\rangle$ to the excited state $|F' = 0, m_{F'} = 0\rangle$, and a π -polarized probe field that coupled the central ground state $|F = 1, m_F = 0\rangle$ to the excited state $|F' = 0, m_{F'} = 0\rangle$. The fields have Rabi frequencies $(\Omega_{c(S)}^+, \Omega_{c(S)}^-)$, and (Ω_p^π) , respectively. These fields result in two DSPs with corresponding wave functions: [17, 18]

$$\psi^+(z, t) = \cos \theta_1(t) \Omega_p^\pi(z, t) - \sin \theta_1(t) \sqrt{N} \rho_{-1,0}(z, t) \quad (32)$$

$$\psi^-(z, t) = \cos \theta_2(t) \Omega_p^\pi(z, t) - \sin \theta_2(t) \sqrt{N} \rho_{0,1}(z, t), \quad (33)$$

with corresponding atomic coherences $\rho_{-1,0}$ and $\rho_{0,1}$.

The mixing angles are expressed as:

$$\cos \theta_1(t) = \frac{\Omega_{c(S)}^+(t)}{\sqrt{|\Omega_{c(S)}^+(t)|^2 + g^2 N}}, \quad \text{and} \quad \sin \theta_1(t) = \frac{g\sqrt{N}}{\sqrt{|\Omega_{c(S)}^+(t)|^2 + g^2 N}} \quad (34)$$

$$\cos \theta_2(t) = \frac{\Omega_{c(S)}^-(t)}{\sqrt{|\Omega_{c(S)}^-(t)|^2 + g^2 N}}, \quad \text{and} \quad \sin \theta_2(t) = \frac{g\sqrt{N}}{\sqrt{|\Omega_{c(S)}^-(t)|^2 + g^2 N}} \quad (35)$$

By adiabatically turning off the control fields $\Omega_{c(S)}^\pm$, the dark state polaritons given in equations (32), and (33) get stored in the form of atomic coherences ($\rho_{-1,0}$, and $\rho_{0,1}$). While these coherences are stored, they evolve with time and pick up equal and opposite dynamic phases in presence of a magnetic field along the quantization axis. At a later time when the control fields $(\Omega_{c(R)}^+, \Omega_{c(R)}^-)$ are turned back on, the atomic coherences are mapped back onto an optical pulse in the original probe pulse direction.

The corresponding retrieved optical pulse (Ω_R) can thereby be expressed as:

$$\Omega_R(t + \tau) \propto \sqrt{N} [\cos \theta_3(t) \rho_{-1,0}(z, t + \tau) + \cos \theta_4(t) \rho_{0,1}(z, t + \tau)] \quad (36)$$

$$= \sqrt{N} e^{-\tau^2 \Gamma_d^2 / 4} [\cos \theta_3(t) \rho_{-1,0}(z, t) e^{-i\phi_-} + \cos \theta_4(t) \rho_{0,1}(z, t) e^{-i\phi_+}], \quad (37)$$

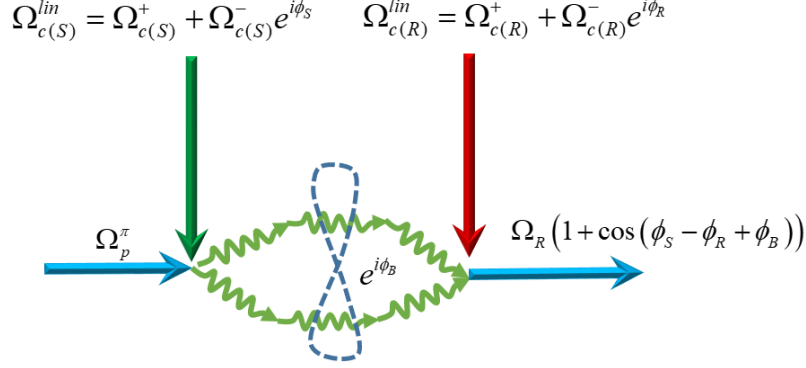


Figure 8. A diagrammatic representation of the equivalent atom-photon interferometer, corresponding to the experiments reported here, with two stored DSPs (shown with green curvy arrows). All other symbols have usual meaning as defined in the main text. The output of the interferometer depends on the relative dynamic phase difference ($\phi_S - \phi_R + \phi_B$) of the two polaritons.

where Γ_d is the Doppler timescale corresponding to a Gaussian decay while the time evolution of $|F = 1, m_F = -1\rangle$ and $|F = 1, m_F = 1\rangle$ in presence of magnetic field B_z (along the quantization axis) results in the dynamic phase $\phi_{\pm} = \frac{\mu_B m_F g_F B_z \tau}{\hbar}$. Here μ_B, m_F , and g_F are Bohr magneton, magnetic quantum number of the respective state, and hyperfine Landé g-factor, respectively. The total relative dynamic phase is then $\phi_- - \phi_+ = \frac{\mu_B B_z \tau}{\hbar} = 2\Delta\tau$, where $g_F = -\frac{1}{2}$ and $\Delta = \frac{\mu_B B_z}{2\hbar}$.

In equation (37) the weights of the contributions from the two coherences in the retrieved pulse are

$$\cos\theta_3(t) = \frac{\Omega_{c(R)}^+(t)}{\sqrt{|\Omega_{c(R)}^+(t)|^2 + g^2 N}}, \text{ and } \cos\theta_4(t) = \frac{\Omega_{c(R)}^-(t)}{\sqrt{|\Omega_{c(R)}^-(t)|^2 + g^2 N}}. \quad (38)$$

Also, $\rho_{12}(z, t) \propto \Omega_{c(S)}^+(z, t)$ and $\rho_{23}(z, t) \propto \Omega_{c(S)}^-(z, t)$. For the special case, $|\Omega_{c(R)}^+(t)| = |\Omega_{c(R)}^-(t)| = |\Omega_{c(S)}^+(t)| = |\Omega_{c(S)}^-(t)| = |\Omega_c(t)|$, the recovery pulse intensity can be expressed as,

$$I_R \propto |\Omega_R(t + \tau)|^2 \propto |\Omega_c|^2 e^{-\tau^2 \Gamma_d^2 / 2} \cos^2 \frac{1}{2}(\phi_c + 2\Delta\tau). \quad (39)$$

Here $\phi_c = \phi_S - \phi_R$, where ϕ_S is the phase difference between $\Omega_{c(S)}^+$ and $\Omega_{c(S)}^-$, and ϕ_R between $\Omega_{c(R)}^+$ and $\Omega_{c(R)}^-$ (Fig. 8). In our experiments we kept $\phi_R = 0$, so that $\phi_c = \phi_S$ becomes the tone phase. Figure 8 depicts a diagrammatic way of representing interference of the two DSPs in the medium. The experiment effectively can be represented as an atom-photon interferometer, with the stored DSPs (light green curvy arrow) are generated in the medium when a linearly polarized control field $\Omega_{c(S)}^{lin}$ (green arrow, composed of two circularly polarized light $\Omega_{c(S)}^{\pm}$) is adiabatically turned off. Generation of the DSPs thereby constitute the first “beam splitter” while the two stored DSPs constitutes the two arms of the interferometer. In presence of a magnetic field (B_z , along the quantization axis), the two polaritons acquire equal and opposite dynamic phases. The resulting relative phase difference of the two arms of the interferometer leaves its signature in the retrieved pulse intensity, using a second linearly polarized control field $\Omega_{c(R)}^{lin}$ (red arrow, composed of two circularly polarized light $\Omega_{c(R)}^{\pm}$). This second control field constitute the second “beam splitter”. While the DSPs are stored in atoms, in presence of anisotropic decay channels γ_g and γ_d , the relative phase of the interferometer gets *locked* to the total phase that includes the relative phase of the beam splitters (the phase difference between the two sets of storing and retrieving control fields) and the phase due to an applied magnetic field. This is the primary physical manifestation of quantum synchronization.

S.IV. Experimental Details:

In this section we discuss the details of some of the experimental techniques used. These include a discussion of experimental timing sequence of events, estimation of temperature of the laser-cooled atoms, calibration of magnetic field, and methods of engineering incoherent decay rates.

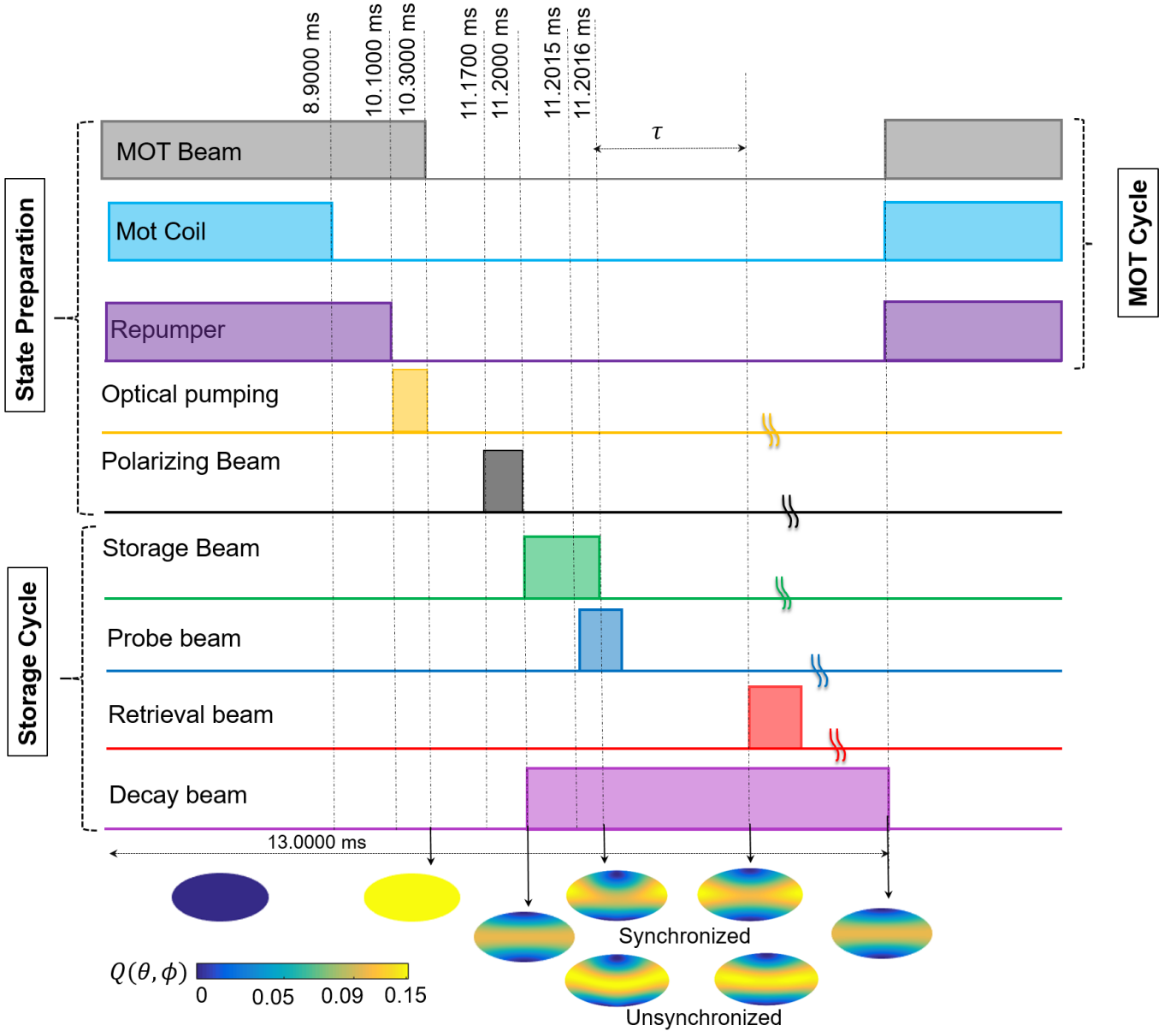


Figure 9. A cartoon of timing sequence for the entire experiment, including state preparation, storage cycle comprising of control, probe and decay fields. For reference, the corresponding numerically simulated spin-1 atomic state, represented by Husimi-Q functions, are shown at different time instances of the experiment.

(a) MOT Cycle:

Figure 9 shows a cartoon diagram corresponding to the timing sequence of one typical experiment, which is repeated over to gather statistics. The repetition rate is 13 ms, with one experimental run includes laser cooling and trapping atoms in a magneto-optics trap (MOT), then optically pumping the atoms to the initial state $|2\rangle = |F = 1, m_F = 0\rangle$ with or without a magnetic field (B_z) and decay beams for γ_g and γ_d , and then storing and retrieving probe pulses by turning on and off the control fields. During the MOT cycle ^{87}Rb atoms are cooled and trapped in $|F = 2\rangle$ hyperfine manifold. After trapping and further cooling the atoms with few ms of polarization gradient cooling (PGC) we start the cycle of storage of the probe pulse. Before it starts, we ensure all the cooling and trapping beams as well as the MOT coil currents are turned off and the resulting fields are nulled.

All this takes 10.1 ms: at 8.9 ms, the MOT coil currents are turned off to let enough time for ringing down of the trapping magnetic fields- at 9.8 ms, the frequency of the MOT beams is decreased by ~ 80 MHz for efficiently pumping the atoms from $|F = 2\rangle$ to $|F = 1\rangle$ - at 10.1 ms, the repumper field ($|F = 1\rangle \rightarrow |F' = 2\rangle$) is turned off and a near

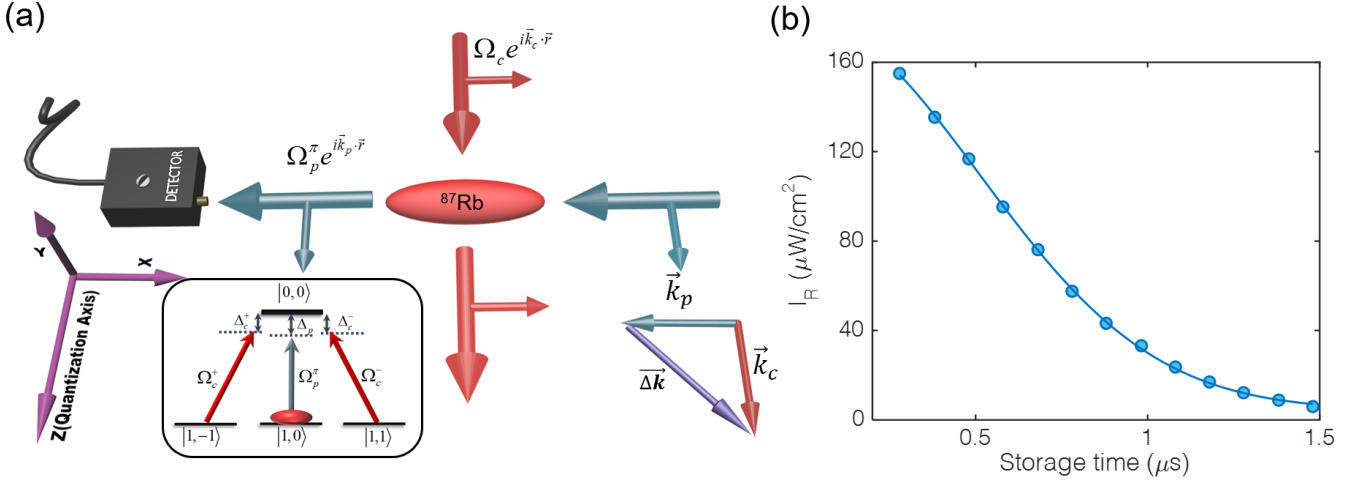


Figure 10. (a) Simplified schematic of a typical storage experiment, where a linear polarized control field (red), comprising of two circularly polarised fields, is perpendicular to a π -polarized probe field. The resulting phase(momentum) mismatch $\Delta\vec{k}$ is shown for the fields. Inset: a schematic of four-level system is shown along with the control and probe field. (b) Experimental data of retrieved intensity as a function of storage time, with $\Delta = 0$. The decaying retrieved pulse intensity is fitted to a Gaussian function ($ae^{-\tau^2/2\tau_d^2}$) of width $\tau_d \approx 510$ ns. From the fitting, effective temperature of the atoms are estimated to be 121 μ K. Here, I_R : retrieved pulse intensity, I_i : input probe pulse intensity

resonant optical beam ($|F = 2\rangle \rightarrow |F' = 2\rangle$) is turned on for 200 μ s to optically pump the atoms to $|F = 1\rangle$ ground state- all the beams are then turned off at 10.3 ms- in the dark, stray magnetic fields are cancelled with X,Y and Z bias coils- at 11.170 ms (at this instance the timing shifts to digital FPGA board with ns timing resolution from DAQ analog control), after shimming the magnetic fields, two orthogonal circular polarized light beams are turned on for 10 μ s: the fields are near resonant from $|F = 1, m_F = -1\rangle \rightarrow |F' = 0, m_{F'} = 0\rangle$ and $|F = 1, m_F = 1\rangle \rightarrow |F' = 0, m_{F'} = 0\rangle$. This completes the initialization of the atomic states, preparing the atoms in $|F = 1, m_F = 0\rangle$ ground state. The state preparation beams are turned off at 11.2 ms, and the storage cycle starts. In the storage cycle, a π -polarised probe pulse of 250 ns is turned on after 1.5 μ s. A linearly polarized control field (composed of left and right circularly polarized fields) is turned on at the beginning of the storage cycle and is turned off at 1.6 μ s in the storage cycle. The process of adiabatic turn off of the control field stores the probe pulse in the form of DSPs. After a controllable time, another linear polarized control field is turned on to read out the stored pulse. By changing the angle of polarization of the storing control field with respect to this retrieval field, we control the tone phase ϕ_c .

To engineer the incoherent decays from ground state $|F = 1, m_F = -1\rangle \rightarrow |F = 1, m_F = 0\rangle$ (γ_g) and $|F = 1, m_F = 1\rangle \rightarrow |F = 1, m_F = 0\rangle$ (γ_d), we use two red detuned (4 MHz) left and right circularly polarized fields that are deliberately phase mismatched by an angle with respect to the control fields. These counter propagating fields, inducing transition between the states $|F = 1, m_F = -1\rangle \rightarrow |F' = 0, m_{F'} = 0\rangle$ and $|F = 1, m_F = 1\rangle \rightarrow |F' = 0, m_{F'} = 0\rangle$ are kept on for 3 μ s, from the beginning of the storage cycle. We set the total time of the storage experiment to 500 μ s: in this timescale, we do not observe any atom loss due to radiation pressure of imbalanced control fields.

Numerically reconstructed states and the corresponding Husimi-Q functions for each time instances are plotted in Fig. 9. Initially, ^{87}Rb atoms are cooled and trapped into $|F = 2\rangle$ ground state in MOT cycle left with no atoms in $|F = 1\rangle$ manifold at around 9.8 ms. After the atoms are optically pumped to ground state $|F = 1\rangle$, the uniformly distributed atoms then correspond to uniform Q over the entire surface of the sphere. At around 11.170 ms we turn on the polarizing beams (composed of two circularly polarized laser fields that are resonant from $|F = 1, m_F = \pm 1\rangle$ to $|F' = 0, m_{F'} = 0\rangle$) to prepare the atoms in the initial state $|F = 1, m_F = 0\rangle$. This state corresponds to equatorial limit cycle. The corresponding Q function is distributed uniformly over all ϕ but centred around $\theta = \pi/2$. At 11.2 ms the main experimental sequence, corresponding to the storage of probe pulse, starts. During this sequence, we observe that for symmetric decay rates, when the DSPs interfere destructively, the Q function remains distributed uniformly over ϕ . However, the asymmetric decay rates induce synchronization, where the atomic, quantum phase ϕ locks to the tone phase of the classical, two photon drive. Finally, after the probe pulse is retrieved, the atomic state settles back to an equatorial limit cycle.

(b) Doppler effect and storage in perpendicular configuration:

For our experiment (Fig. 10a, inset), we keep the control and probe fields perpendicular to each other (Fig. 10a). This perpendicular geometry results in excellent signal to noise ratio for detecting probe intensity in a direction that remains orthogonal to all other strong control and decay beams. However, such a geometry also results in a large mismatch of the two-photon momentum, causing severe Doppler decoherence. This time can be estimated from the time taken by an atom moving at average thermal velocity, to move over one period of the resulting wave-vector mismatch grating i.e.

$$\tau_d = \frac{\lambda_s/2}{v_{th}}, \quad (40)$$

after substituting λ_s and v_{th} in equation (40) we get

$$\tau_d = \frac{1}{2|\Delta\vec{k}|} \sqrt{\frac{\pi m}{2k_B T}}. \quad (41)$$

From the measured τ_D , we thereby estimate the average thermal velocity and the temperature of the atomic ensemble as:

$$T = \frac{\pi m}{8|\Delta\vec{k}|^2 k_B \tau_d^2}, \quad (42)$$

here $|\Delta\vec{k}|^2 = |\vec{k}_c|^2 + |\vec{k}_p|^2 + 2\vec{k}_c \cdot \vec{k}_p = |\vec{k}_c|^2 + |\vec{k}_p|^2 = 2|\vec{k}_p|^2$, as direction of \vec{k}_p and \vec{k}_c is perpendicular to each other and $|\vec{k}_p| = |\vec{k}_c|$, k_B is the Boltzmann's constant, and τ_d is the decoherence time due to the thermal velocity of atoms. In Fig. 10b the peak of the retrieved pulse intensity with respect to the storage time τ is plotted and fitted with a Gaussian function $a e^{-\tau^2/2\tau_d^2}$, as averaged over Maxwell velocity distribution yields Gaussian decay. From the fitting parameter, we extract $\tau_d \approx 510$ ns. Plugging in the values of τ_d, k_B and $|\Delta\vec{k}|$ in equation (42), we estimate the temperature of the atomic cloud to be $T \sim 121$ μ K.

(c) Magnetic field calibration using interferometric measurement:

As discussed, the two stored DSPs interfere constructively or destructively depending upon the phase difference $\phi_c = \phi_S - \phi_R$. In presence of an applied magnetic field, the generated coherences $\rho_{-1,0}$ and $\rho_{0,1}$ between the states $|F=1, m_F=-1\rangle$, $|F=1, m_F=0\rangle$ and $|F=1, m_F=1\rangle$ acquire additional dynamic phase $2\Delta\tau(2\pi)$ in a finite storage time (τ), where $2\Delta = \Delta_- - \Delta_+$. Accordingly, the intensity of the retrieved pulse depends on the total phase $\phi_c + 2\Delta\tau(2\pi)$. For all our experiments, we keep $\phi_R = 0$ i.e. $\phi_c = \phi_S$. At a fixed magnetic field, we observe interference fringes in time for the retrieved pulse amplitude which we interpret as due to the dynamic phase difference between the two generated DSPs (Fig. 5c). Figure 11b shows the retrieved pulse peak with ϕ_S and measured voltage V_m from the current monitor of the current controller circuit which is used to generate magnetic field along the quantization axis. We use these interference fringes (Fig. 11b) to calibrate the Zeeman shift Δ to the measured voltage V_m at the magnetic field controller. To relate V_m to Δ , we measure the peak of the retrieved pulse amplitude along the black line in Fig. 11b. The peak is observed to depend on the total relative phase $\phi_S + 2\Delta\tau(2\pi) = 0$ between the two stored coherences or DSPs. Here the measured voltage (V_m) correspond to the dynamic phase $2\Delta\tau(2\pi)$. Along the black locus, the total change in ϕ_c (y-axis) and measured voltage V_m (x-axis) are 480° and 364 mV, respectively. So the equivalent change in phase per mV is $\frac{d\phi_S}{dV_m} = 0.023$ rad/mV. Accordingly, the acquired dynamic phase can be written as:

$$4\pi\Delta\tau = \frac{d\phi_S}{dV_m} V_m \text{ rad}. \quad (43)$$

After rearranging the terms we find:

$$\Delta = \frac{0.023}{4\pi\tau} V_m \text{ MHz}, \quad (44)$$

where V_m is in mV.

(d) Engineering decay channels:

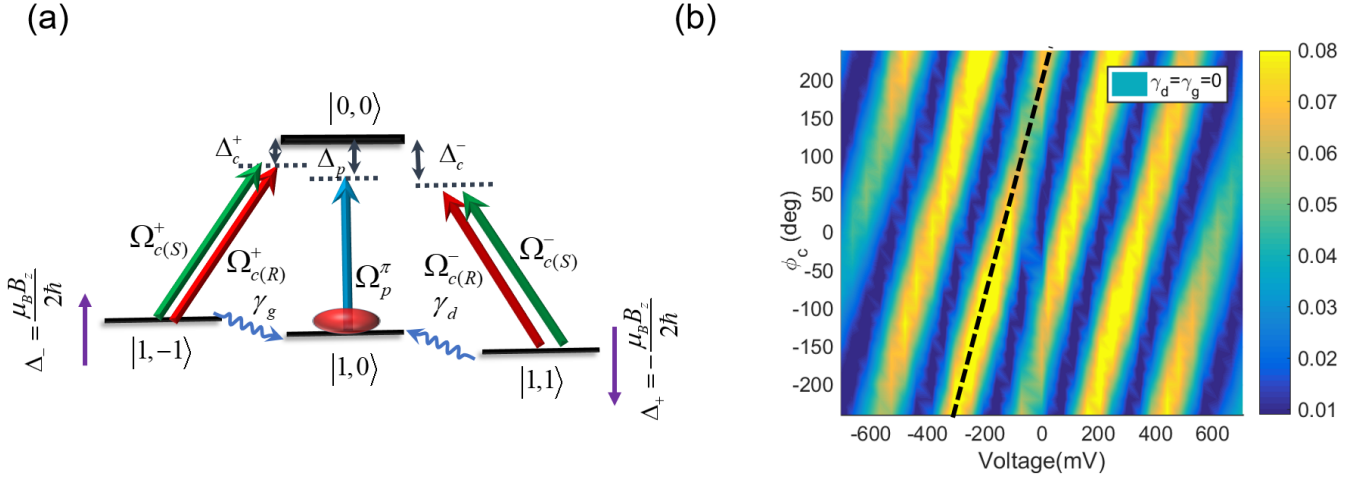


Figure 11. (a) Atomic energy level scheme of the 4-level system. A π -polarized Probe Ω_p^π (blue) is stored with a linearly polarized control field $\Omega_{C(S)}^{\text{lin}}$ (green) composed of two orthogonal circularly polarized fields $\Omega_{c(S)}^+$ and $\Omega_{c(S)}^- e^{i\phi_S}$, and retrieved by another linearly polarized control field $\Omega_{C(R)}^{\text{lin}}$ (red) (composed of $\Omega_{c(R)}^+$ and $\Omega_{c(R)}^- e^{i\phi_R}$). The dynamic phase ($\Delta_- - \Delta_+$) between the two dark state polaritons which are stored in the medium is due to an applied magnetic field B_z along the quantization axis. (b) Peak of the retrieved pulse intensity at retrieval time ($\tau = 600$ ns) is plotted with applied magnetic field (measured voltage due to the current through the coils) and control phase $\phi_c = \phi_S - \phi_R$, here we set $\phi_R = 0$. We observe fringes due to interference between the two dark state polaritons. The slope of the black dotted line is used to calibrate the magnetic field and thereby, the dynamic phase ($\Delta_- - \Delta_+$).

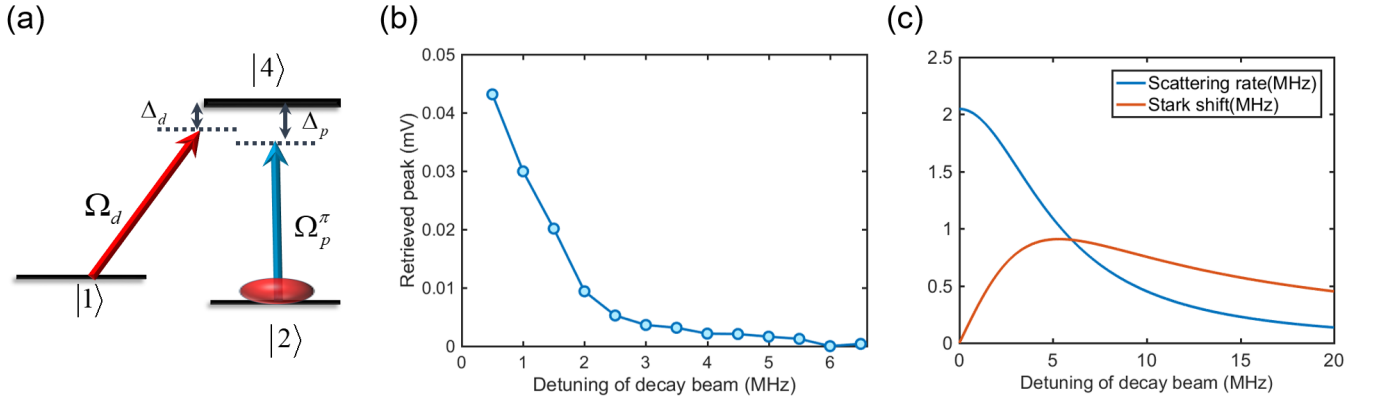


Figure 12. (a) A schematic of the experiment to test induced coherence of the decay beams, with Ω_d as the decay beam along with a probe field Ω_p^π . We mimic a storage and retrieval experiment by turning on and off the decay field. The resulting retrieved pulse is plotted in (b) as a function of the detuning Δ_d of the decay beam. From this plot, we choose $\Delta_d = 4$ MHz, where the retrieval, and thereby the induced coherence is less than 3%. For a larger choice of Δ_d , the decay rates γ_g and γ_d decreases significantly, as is shown the theoretical plots in (c).

The decay beams (Fig. 1b, main text) in the main text are used to create a stable equatorial limit cycle in a *spin-1* system (Fig. 1, main text). These incoherent decays are generated from two lasers, 4 MHz red detuned from $|F' = 0\rangle$, counter propagating and are left and right circularly polarized. Deliberate phase mismatch from the control and counter propagation ensures minimal generation of coherence [2] between $|F = 1, m_F = 1\rangle$ and $|F = 1, m_F = -1\rangle$ states.

However, in presence of probe, these fields can also independently generate ground state coherences $\rho_{-1,0}$ and $\rho_{0,1}$ in a EIT scenario. To avoid such a situation, we break the two-photon resonance condition for such processes by maintaining these beams red detuned from the probe by 4 MHz. To ensure this, we perform a typical storage experiment with π -polarized probe beam, and each of these circularly polarized decay beams (Fig. 12a). Here the states $|1\rangle$, $|2\rangle$ and $|4\rangle$ correspond to $|F = 1, m_F = 1\rangle$, $|F = 1, m_F = 0\rangle$, and $|F' = 0, m_{F'} = 0\rangle$, respectively. We keep the probe frequency resonant to the excited state and change the detuning of the decay beam. Fig. 12b shows the

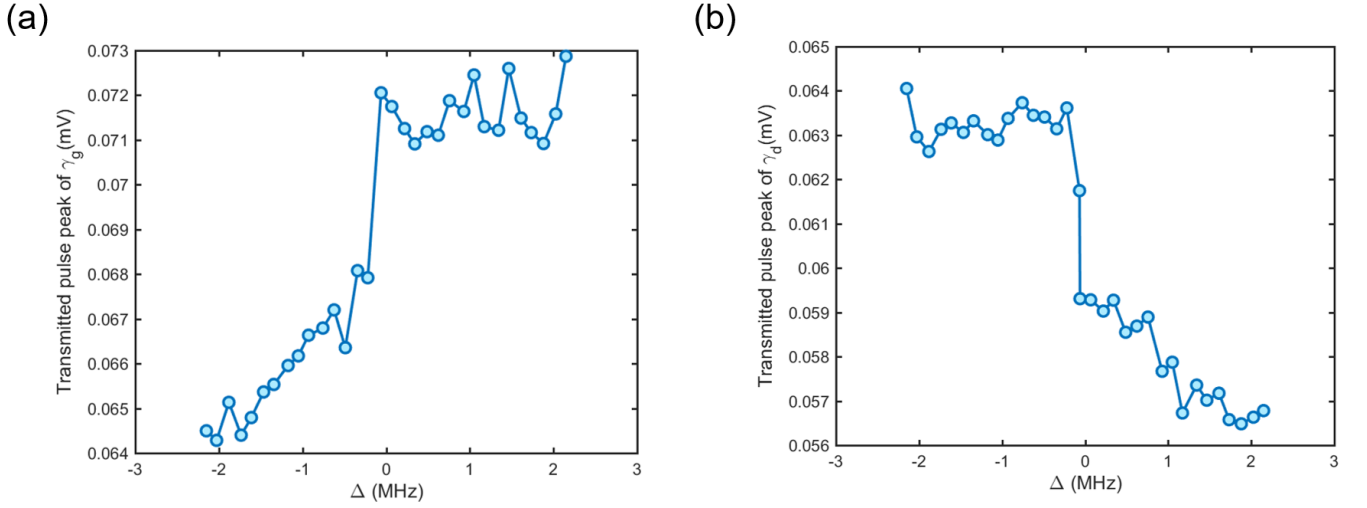


Figure 13. (a) Transmission of decay beam γ_g as a function of magnetic field (Δ) which results in effective change in detuning with respect to excited state $|F' = 0, m_{F'} = 0\rangle$. (b) Same data but for γ_d . We use this data, to keep the detuning of the decay rates constant, by actively compensating shift due to an applied magnetic field.

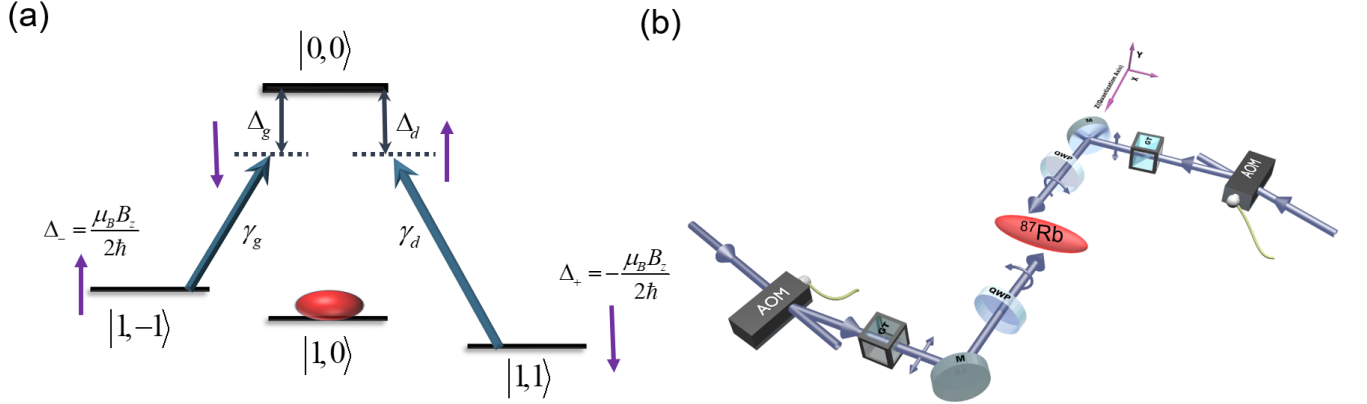


Figure 14. (a) With increasing magnetic field in positive direction $|1, -1\rangle$ shifts upwards resulting into $\Delta_g < 4$ MHz, and the state $|1, 1\rangle$ shifts downwards resulting $\Delta_d > 4$ MHz. So, the detuning of decay beams γ_g and γ_d are kept fixed at 4 MHz by increasing and decreasing the detuning of the respective beams by tuning the AOMs drive frequency. (b) Schematic of experimental setup for decay beams. AOM: Acousto-Optic Modulator; GT: Glan-Thompson polarizing beam splitter; M: Mirror; QWP: Quarter-Wave Plate.

retrieved pulse peak with decay beam detuning. The detuning is increased to the red side of the excited state. The strength of the decay beam is $\Omega_d/\gamma = 1.01$, where γ is the excited state decay. The plot shows that after 3 MHz detuning, the retrieval efficiency has gone down significantly. The decay beams then essentially scatters atoms and introduce stark shifts of ground state levels. The scattering rates (R_{sc}) and stark shifts (Δ_{ss}) due to this beam can be estimated from [19, 20]:

$$R_{sc} = \frac{\Gamma}{2} \frac{I/I_{sat}}{1 + 4(\delta/\Gamma)^2 + I/I_{sat}}, \quad (45)$$

and

$$\Delta_{ss} = \frac{\delta}{2} \frac{I/I_{sat}}{1 + 4(\delta/\Gamma)^2 + I/I_{sat}}, \quad (46)$$

respectively.

In Fig. 12c the scattering rates and stark shifts are plotted with detuning (Δ_d). We find a red detuning of 4 MHz to be optimum choice, where the coherence falls down to less than few percent while the scattering rate still remains

substantial with a fall of 50%, at this value of the detuning. Further increase of detuning leads to significant decrease in scattering rates. We keep the detuning of decay compensating beam at 4 MHz throughout the experiment.

It can be noted that changes in magnetic field leads to ground state energy shifts (Δ) which change the detuning of the decay beam from 4 MHz. Accordingly, scattering rate due to these beams also change. To keep the scattering rate constant, the detuning of these beams are adjusted to keep them at 4 MHz red detuned from the excited state. With positive applied magnetic field the detuning between $|1, -1\rangle$ and $|0, 0\rangle$ reduces whereas detuning corresponding to $|1, 1\rangle \rightarrow |0, 0\rangle$ enhances. To compensate for the change in detuning of decay beams, it is important to identify the exact polarization of two beams, and with the help of this information, we can adjust the detuning of beams accordingly. To identify in which direction the detuning must be compensated, we perform an experiment by observing the absorption of these decay beams with changing magnetic field by labelling them as γ_g and γ_d . The transmitted peaks of γ_g and γ_d pulses are plotted with respect to detuning in Fig. 13a and b, respectively. It can be observed from Fig. 13a that the absorption is increasing in the negative Δ side in case of γ_g , and it is identified as right circularly polarized light. With a similar argument, γ_d is identified as left circularly polarized light (Fig. 13b). As we change the detuning of the system from -2.15 MHz to 2.15 MHz, the effective detuning of γ_g is fixed at 4 MHz by adjusting the detuning of the beam from $(4 + 2.15) = 6.15$ MHz to $(4 - 2.15) = 1.85$ MHz, and for γ_d the change is opposite (Fig. 14a). The detuning of the beams are adjusted by changing the AOM drive frequency. We derive these decay beams from a single laser which is locked using beat note lock technique [21]. The output of the laser is divided into two paths and send through acousto-optic modulators (AOMs) for switching the intensities. The first order of the blue shifted beams from these AOMs are used as the decay beams (Fig. 14b). These beams are resonant to the excited state $|F' = 0\rangle$ when the AOMs are driven with 80 MHz RF sources. Here, we adjust the scattering rates (γ_g, γ_d) by controlling the frequencies and amplitude of RF signal which drive these AOMs.

* gsaikat@iitk.ac.in

- [1] R. Grobe, F. T. Hioe, and J. H. Eberly, Phys. Rev. Lett. **73**, 3183 (1994).
 - [2] A. W. Laskar, N. Singh, A. Mukherjee, and S. Ghosh, New Journal of Physics **18**, 053022 (2016).
 - [3] A. W. Laskar, N. Singh, P. Adhikary, A. Mukherjee, and S. Ghosh, Optica **5**, 1462 (2018).
 - [4] T. E. Lee and H. R. Sadeghpour, Phys. Rev. Lett. **111**, 234101 (2013).
 - [5] M. Koppenhöfer and A. Roulet, Phys. Rev. A **99**, 043804 (2019).
 - [6] K. Husimi, Proceedings of the Physico-Mathematical Society of Japan. 3rd Series **22**, 264 (1940).
 - [7] A. Roulet and C. Bruder, Phys. Rev. Lett. **121**, 053601 (2018).
 - [8] J. M. Radcliffe, Journal of Physics A: General Physics **4**, 313 (1971).
 - [9] Y. Lee Loh and M. Kim, American Journal of Physics **83**, 30 (2015).
 - [10] S. Walter, A. Nunnenkamp, and C. Bruder, Annalen der Physik **527**, 131 (2015).
 - [11] D. M. Goldberg and J. R. Gott, Cartographica: The International Journal for Geographic Information and Geovisualization **42**, 297 (2007).
 - [12] M. Fleischhauer and M. D. Lukin, Phys. Rev. Lett. **84**, 5094 (2000).
 - [13] D. F. Phillips, A. Fleischhauer, A. Mair, R. L. Walsworth, and M. D. Lukin, Phys. Rev. Lett. **86**, 783 (2001).
 - [14] M. Fleischhauer and M. D. Lukin, Phys. Rev. A **65**, 022314 (2002).
 - [15] M. D. Lukin, Rev. Mod. Phys. **75**, 457 (2003).
 - [16] M. Fleischhauer, A. Imamoglu, and J. P. Marangos, Rev. Mod. Phys. **77**, 633 (2005).
 - [17] H. Wang, S. Li, Z. Xu, X. Zhao, L. Zhang, J. Li, Y. Wu, C. Xie, K. Peng, and M. Xiao, Phys. Rev. A **83**, 043815 (2011).
 - [18] L. Karpa, F. Vewinger, and M. Weitz, Phys. Rev. Lett. **101**, 170406 (2008).
 - [19] D. A. Steck, "Rubidium 87 D line data, available online at <http://steck.us/alkalidata>,".
 - [20] C. N. Cohen-Tannoudji, Rev. Mod. Phys. **70**, 707 (1998).
 - [21] U. Schünemann, H. Engler, R. Grimm, M. Weidemüller, and M. Zielonkowski, Review of Scientific Instruments **70**, 242 (1999).
-